PNAS

Supplementary Information for
Reconstructing river flows remotely on Earth, Titan, and Mars.

*Samuel P.D. Birch, *Gary Parker, Paul Corlies, Jason M. Soderblom, Julia W. Miller, Rose V. Palermo, Juan M. Lora, Andrew D. Ashton, Alexander G. Hayes, and J. Taylor Perron

*Samuel Birch & Gary Parker
Email: sbirch@mit.edu & parkerg@illinois.edu

This PDF file includes:

Supplementary text
Figures S1 to S5
Tables S1 to S6
References

Other supplementary materials for this manuscript include the following:

Dataset S1

Supplementary Text

1. Dependence of hydraulic geometry coefficients on sediment and fluid density

1.1. Bedload-Dominated Rivers

To account explicitly for the fluid and sediment properties (3) embedded within the four scaling coefficients (α_i's) in Equation 1, Parker et al. (1) sought four equations that described how channel properties of bedload-dominated (i.e., gravel) rivers adjust to changing discharge.

Following Parker (3), the resistance to flow in the channel is described through the Manning-Strickler resistance relation (1),

$$\frac{u}{u^*} = \frac{Q}{BH\sqrt{gHS}} = \alpha_r \left(\frac{H}{D_{50}}\right)^{n_r} \quad , \tag{16}$$

where α_r and n_r are physical constants that will be calibrated from the empirical fits to terrestrial rivers. This also introduces gravity through the friction velocity, something that is replicated in our initial non-dimensionalization (i.e., scaling by $g^{0.5}$ in Equations 1d and 1e). To describe the bed shear stress needed to mobilize sediment, Parker (3) employed the Shields (1,3) relation

$$\tau_c^* = \frac{HS}{RD_{50}} = r\alpha_\tau \hat{Q}^{n_\tau} \quad , \tag{17}$$

where τ^* is the Shields number ($\tau^* = \frac{HS}{RD_{50}}$) and *r*

$$r = \frac{\tau^*}{\tau_c^*} = 1.63 \quad , \tag{18}$$

which is part of the Parker et al. (1,22) theory for the width of rectangular channels with mobile bed and banks. Specifically, the Parker et al. (1,22) theory posits that channel width adjusts to increasing/decreasing discharge by widening/narrowing such that the shear stress at the channel banks is just below the critical shear stress. For a rectangular channel, this implies the shear stress at the channel center line is slightly greater than the critical shear stress, permitting the transport of bedload downstream. Though additional factors can influence channel width (26), especially cohesion, our work is likely on even firmer grounds on Mars or Titan (see the arguments presented in the main text). The constants α_τ and n_τ in Equation 17 are additional physical constants, while $R = \frac{\rho_s}{\rho} - 1$ relates the fluid density (ρ) to the sediment density (ρ_s).

The third and fourth equations from Parker et al. (1) are the Parker-Einstein equation (1,3) and a sediment "yield" equation (1,3), which both describe the transport of bedload sediment within threshold bedload-dominated rivers. Both are related to the dimensionless bedload transport rate ($\hat{Q}_s$) according to

$$\hat{Q}_s = \frac{\beta_y}{1+R}\left(\frac{Q}{D_{50}^2\sqrt{gD_{50}}}\right)^{n_y} = \frac{\alpha_g}{R}\frac{B}{D_{50}}\left(\frac{HS}{D_{50}}\right)^{3/2}\left(1-\frac{1}{r}\right)^{4.5} \quad . \tag{19}$$

The second term in Equation 19 is the gravel yield relation (1,20), while the third term is the Parker-Einstein relation (1,3). Additional physical constants are introduced in Equation 19: $\alpha_g \equiv 11.2$ is a fixed empiricism for bedload-dominated rivers (1,3), and β_y scales a river's fluid discharge to a sediment flux (3).

Substituting the dimensionless hydraulic geometry relations from Equation 1 into Equations 16–18, we derive expressions that relate the physical α's and *n*'s to the empirical α's and *n*'s via *R*:

$$\alpha_\tau = \frac{\alpha_h \alpha_s}{rR}\,, \qquad \alpha_r = \frac{1}{\alpha_b \alpha_s^{0.5} \alpha_h^{1.5+n_r}}\,, \qquad \alpha_y = \frac{\alpha_g \left(1-\frac{1}{r}\right)^{4.5} \alpha_b \alpha_h^{1.5} \alpha_s^{1.5}}{R} = \frac{\beta_y}{1+R} \quad , \tag{20}$$

and

$$n_\tau = n_h + n_s + \frac{2}{5} \quad , \qquad n_r = -\frac{(n_b + 1.5n_h + 0.5n_s)}{n_h + 0.4}\,, \qquad n_y = n_b + \frac{3}{2}(n_s + n_h) + 1 \ . \tag{21}$$

We then used the empirical fits (Table S2) to the subset of bedload-dominated rivers with floodplains to supply the constants in Equations 20 and 21, with R = 1.65 for Earth, to calculate the values of the physical α's and n's:

$$\alpha_\tau = 0.01\,, \qquad \alpha_r = 2.9\,, \qquad \alpha_y = 0.004 \quad , \tag{22}$$

and

$$n_\tau = 0.05 \quad , \qquad n_r = 0.36\,, \qquad n_y = 0.53 \quad . \tag{23}$$

We then re-cast Equations 20–21 so as to have the empirical α's as functions of both R and the Earth-calibrated physical α's and n's:

$$\alpha_h = \left(\frac{(1+R) r \alpha_\tau \alpha_g \left(1-\frac{1}{r}\right)^{4.5}}{\beta_y \alpha_r} \right)^{\frac{1}{1+n_r}}\,,$$

$$\alpha_s = rR\alpha_\tau \left(\frac{(1+R) r \alpha_\tau \alpha_g \left(1-\frac{1}{r}\right)^{4.5}}{\beta_y \alpha_r} \right)^{\frac{-1}{1+n_r}}\,,$$

$$\alpha_b = \frac{\beta_y}{(1+R)\sqrt{R}(r\alpha_\tau)^{1.5} \alpha_g \left(1-\frac{1}{r}\right)^{4.5}} \quad . \tag{24}$$

Substituting the numerical values from Equations 22 and 23 into Equation 24 yields the desired dependence of the empirical hydraulic geometry coefficients on R:

$$\alpha_b = \frac{18}{(1+R)\sqrt{R}}, \qquad \alpha_h = 0.22(1+R)^{0.73}, \qquad \alpha_s = \frac{0.11R}{(1+R)^{0.73}}, \qquad \alpha_y = \frac{0.01}{(1+R)} \quad . \tag{25}$$

Equation 25 is included in the main text as Equation 2.

1.2. Suspended Load-Dominated Rivers

We performed a similar analysis for suspended load-dominated rivers following the work of Wilkerson & Parker (2). While broadly similar to the analysis of bedload-dominated rivers, differences arise in the adopted relation for the sediment yield. Whereas Parker et al. (1) used a relation for bedload transport at bankfull flow described by Equation 19, Wilkerson & Parker (2) instead adopted the Engelund-Hansen (2) formulation to estimate the total sediment load at bankfull flow,

$$\hat{Q}_t = \alpha_y \hat{Q}^{n_y} = \frac{\alpha_e}{R^{m_e - 0.5}} \frac{\hat{Q}^{0.4(m_e+1)}}{\tilde{B}\tilde{H}^{3-m_e} S^{1-m_e}} \ , \tag{26}$$

which introduces two new empirical constants, $\alpha_e = 0.05$ and $m_e = 2.5$. Note that the physical constants in Equation 26 (α_y and n_y) are for suspended load-dominated rivers, and their values differ from those for bedload-dominated rivers. From Wilkerson & Parker (2), we again related the physical α's and n's to the empirical α's and n's via R as we did for Equations 20 and 21:

$$\alpha_\tau = \frac{1}{R}\beta_h \beta_s\,, \qquad \alpha_r = \frac{1}{\beta_b \beta_s^{0.5} \beta_h^{1.5+n_r}}, \qquad \alpha_y = \frac{\alpha_e}{R^{m_e-0.5}} \frac{\beta_h^{m_e-3} \beta_s^{m_e-1}}{\beta_b} \quad , \tag{27}$$

and

$$n_\tau = n_h + n_s + \frac{2}{5} \quad , \quad n_r = -\frac{5(2n_b+3n_h+n_s)}{2(5n_h+2)}, \quad n_y = 0.4 - (n_b + 3n_h + n_s) + m_e(0.4 + n_h + n_s) \quad , \tag{28}$$

where β_i (representing β_b, β_h, β_s) is defined as

$$\beta_i = \alpha_i Re_p^{m_i} \ . \tag{29}$$

Equations 27 and 28 are analogous to Equations 20 and 21, with modifications to the sediment transport terms (α_y and n_y) and the inclusion of Re_p throughout. As before, we substituted the empirically fitted α's, n's, and m's to calculate the numerical values of the quantities in Equations 27 and 28 as

$$\alpha_\tau = 0.050 Re_p^{-0.16} \ , \quad \alpha_r = 0.96 Re_p^{0.11}, \quad \alpha_y = 3.6 \times 10^{-5} Re_p^{-0.12} \ , \tag{30}$$

and

$$n_\tau = 0.17 \quad , \quad n_r = 0.21, \quad n_y = 1.1 \quad . \tag{31}$$

Finally, we re-cast Equations 27 and 28, as we did for bedload-dominated rivers, to express the empirical β's as functions of both R and the Earth-calibrated physical α's, n's, and m's:

$$\begin{aligned} \beta_h &= \left(\alpha_\tau \left(\frac{\alpha_y}{\alpha_r \alpha_e}\right)^{-0.5}\right)^{\frac{1}{0.5-n_r}}, \\ \beta_s &= R\alpha_\tau \left(\alpha_\tau \left(\frac{\alpha_y}{\alpha_r \alpha_e}\right)^{-0.5}\right)^{-\frac{1}{0.5-n_r}}, \\ \beta_b &= \frac{1}{\sqrt{R}} \frac{1}{\alpha_r \alpha_\tau^{0.5}} \left(\alpha_\tau \left(\frac{\alpha_y}{\alpha_r \alpha_e}\right)^{-0.5}\right)^{-\frac{1+n_r}{0.5-n_r}}, \end{aligned} \tag{32}$$

which are less compact than the equivalent forms in Equation 25 because they additionally include Re_p through the physical α's (Equation 30). Substituting Equations 30 and 31 into Equation 32 and using Equation 29 provides

$$\alpha_b = \frac{0.95}{\sqrt{R}}, \quad \alpha_h = 3.8, \quad \alpha_s = 0.01R, \quad \alpha_y = 3.6 \times 10^{-5} Re_p^{-0.12} \ , \tag{33}$$

which are analogous to the expressions in Equation 25 but correspond to suspended load-dominated rivers. Equation 33 is included in the main text as Equation 3.

2. Additional Information Pertaining to Altimeter Measurements over Vid Flumina

During the T91 flyby of Titan's polar regions, *Cassini* acquired data in altimetry mode for a brief period before, after, and while it crossed Ligeia Mare. This flyby was designed to constrain wave activity on Ligeia Mare. The data were also used to derive the depth and composition of the sea from the two-way travel time of the signal and the relative power of the surface and subsurface reflections (see Hayes et al. (4) for a more detailed review).

Before crossing the sea, the altimeter also received data from the solid surface, providing a topographic profile with ~35 meter vertical precision across the land surface (59). At eight unique points, the altimeter also detected isolated liquids, which clearly differ from the surroundings due to the tremendous power returned to the radar from the flat liquid surfaces (see Figures 1 & 2 in Poggiali et al. (31)). These points correlated with rivers observed in SAR images (31). Because of

the high power returned to the spacecraft over liquids, the elevation of these liquids could be measured to higher precision (31,59).

In Figure S4A, points i, ii, iii, and iv ("e", "f", "g" and "h" respectively in Figure 2 of Poggiali et al. (31)) are of particular interest, as they lie on the Vid Flumina river network. Points i, ii, and iii all lie on parts of the river network closer to the Ligeia Mare coast and have elevations consistent with sea level. This suggests the lower portion of the river network is either flooded, or the slope is extremely gentle. Point iv lies on a tributary farther upstream and is the only one of the four points with an elevation above sea level.

To measure the slope of the channel network, we measured the relief between point iv and the main branch to be 64 meters, assuming that the liquid elevation at the junction is equivalent to the elevation of point iii (Figure 1G and Figure S4A–C). We then divided this relief by the along-channel path length between point iv and the main branch to calculate an average slope. We choose two path lengths. The shorter length (43 km), which yields a steeper slope estimate, extends from point iv to a location upstream of the tributary junction that appears flooded (Figure S4c). The longer path length, which yields a lower slope, extends from point iv to the tributary junction itself (60 km).

The maximum channel width at point iv is measured directly from the SAR image (Figure 1G, Figure S4), which is at the resolution of the instrument (175 m). The minimum channel width is derived from the altimetry data. Specifically, when the altimeter sends out an echo, the projected beam size on the surface is ~12 km, with information from anywhere within this beam footprint being returned to the spacecraft at different times. The Fresnel zone represents the inner ~1% of the beam, and is the diameter wherein a perfectly flat surface would return a coherent specular reflection back to the spacecraft (59). Analyses of the waveforms returned to *Cassini* over these isolated liquids show that the return is specular (31), and therefore the entire Fresnel zone must be occupied by liquid. For the altitude of *Cassini* during its T91 flyby, the Fresnel zone is ~100 m in diameter (59), which implies that the tributary at point iv must be at least 100 meters wide.

3. Dynamic similarity of sediment grain size

Extending the Parker et al. (1) and Wilkerson and Parker (2) theory to Mars and Titan assumes that the sediment grains traveling in bedload-dominated rivers on Mars and Titan are dynamically similar to those on Earth. This requires equivalent values of the dimensionless particle Reynolds number,

$$Re_p = \frac{D_{50}\sqrt{RgD_{50}}}{\nu}, \tag{34}$$

which describes the nature of flow around particles. Dynamical similarity between another planet and Earth then requires

$$\frac{D_{50}}{D_{50,e}} = \left(\frac{\nu}{\nu_e}\right)^{\frac{2}{3}}\left(\frac{R}{R_e}\right)^{-\frac{1}{3}}\left(\frac{g}{g_e}\right)^{-\frac{1}{2}} \sim 1 \quad . \tag{35}$$

Inserting known values for materials on Earth, and our estimated values for Titan and Mars (Table S1), we calculated that dynamically similar water ice sediment on Titan is ~1.3–1.7× larger than quartz sediment on Earth, and that dynamically similar mafic sediment on Mars is ~1.3× larger than quartz sediment on Earth (Figure S5). These small differences imply that the extension of the theory for bedload-dominated rivers on Earth to Mars and Titan is justified.

Our approach also assumes that flow in bedload-dominated transport is fully turbulent (such that τ_c^* is a constant), such that Re_p > ~3000. Indeed, our calculations show (Figure S5) that this is the case on Earth, Mars, and Titan, regardless of our choice of fluid and sediment properties on Titan.

This assumption is unnecessary for suspended load-dominated rivers, which instead are a function of Re_p.

4. Dynamic similarity of sediment transport mode

For our planetary calculations, we assumed a given river type (suspended load-dominated or bedload dominated) and then calculated the resulting bed grain size, flow discharge, sediment flux, and flow depth. For self-consistency, this required that the estimated flows and channel geometries would indeed transport sediment mainly via the assumed mechanism (i.e., as bedload or suspended load). To check this, we calculate the Rouse number (P), a dimensionless number that compares a particle's settling velocity (ω_s) to the fluid's shear velocity (u_*),

$$P = \frac{\omega_s}{u_* \kappa}, \tag{36}$$

where $\kappa = 0.4$ is the von Kármán constant. We express the settling velocity in dimensionless terms (66), with a dimensionless settling velocity W^* and dimensionless particle size D^*

$$W^* = \frac{\omega_s^3}{Rg\nu} \quad , \tag{37}$$

$$D^* = \frac{RgD_{50}^3}{\nu^2} \quad . \tag{38}$$

As described by Dietrich (66), these dimensionless quantities are related by a fourth-order polynomial

$$\begin{aligned} \log_{10} W^* = &-3.76715 + 1.92944(\log_{10} D^*) - 0.09815(\log_{10} D^*)^2 \\ &-0.00575(\log_{10} D^*)^3 + 0.00056(\log_{10} D^*)^4 \quad . \end{aligned} \tag{39}$$

Meanwhile the shear velocity is defined as

$$u_* = \sqrt{gHS} \quad . \tag{40}$$

For each of the reconstructed planetary river flows presented in the manuscript (2 for Peace Vallis, 3 for Jezero, 4 for each of Saraswati Flumina and Vid Flumina), we calculated the shear velocity from Equation 40 using the measured slope and calculated flow depth (Tables S3–6). We then calculated *D** from Equation 38 using the estimated bed grain size (Tables S3–6) and material properties from Table S1. For suspended load-dominated rivers we do not calculate bed grain size, but instead assume a bed grain size of 1.5 mm (our adopted maximum sand grain size), scaled by the relative increase in grain size expected for each planet (1.3× for Mars and 1.3–1.7× for Titan, see Equation 35). Inserting the value of *D** into Equation 39, we calculated *W**, which in turn we used in Equation 37, which we solved for dimensional settling velocity. We then calculated the Rouse number from Equation 36 for each planetary river scenario and compared it with the critical values that delineate different modes of sediment transport.

For $P \gtrsim 2.5$ particles will travel as bedload, as they settle out of the flow faster than they can be lofted by fluid turbulence. For $0.8 \lesssim P \lesssim 2.5$, particles will travel predominantly in suspension. For $P \lesssim 0.8$, particles will be carried predominantly as washload. For nearly all our planetary river scenarios, the calculated Rouse numbers are as expected, with all assumed bedload dominated rivers with $P > 2.5$ and all assumed suspended load-dominated rivers with $P = 0.8 - 2.5$. Only for Saraswati Flumen in the scenario where we assume both the largest width (700 m) and steepest slope (0.002) does our assumption fail ($P \sim 0.5 - 0.7$). However, this may be expected for such a large river carrying relatively buoyant sediment.

Finally, we also calculated the Froude number for all of our planetary rivers,

$$Fr = \frac{u}{\sqrt{gH}} \quad , \tag{41}$$

where u is the flow velocity. For each of our planetary rivers we calculated the flow velocity as $u = Q/(BH)$, the average velocity for a river with a rectangular cross-section, and then the Froude number. We find that all of our rivers are sub-critical ($Fr < 1$), like most of the rivers in our terrestrial dataset.

5. Sources of River Geometry Data

To assemble hydraulic geometry data for a large collection of alluvial rivers on Earth, we leveraged the compilations by Pfeiffer et al. (74), Phillips & Jerolmack (75), Parker et al. (1), and Trampush et al. (76). There was frequent overlap between these datasets, so we manually culled the data to remove duplicates. We only included rivers for which measurements of all five quantities of interest (slope, median bed grain size, and bankfull width, depth, and discharge) were available. We also gathered data for alluvial rivers from Kaless et al. (77), who report on the only non-North American rivers in our dataset.

For ephemeral rivers, we assembled data from the BYU database (36). For bedrock rivers, bed grain size is frequently not reported, yielding a relatively small dataset assembled from the studies of Wohl & David (78), Turowski et al. (79), and the Hanalei river drainage basin in Hawaii (Ferrier et al. (80); Kimberly Huppert, pers. comm.).

Sediment flux data were acquired from the compilation of Hinton et al. (36). Some of the rivers included in the compilation of Hinton et al. (36) are also included in the other compilations we used to assemble the hydraulic geometry dataset. For some of those rivers, channel geometry measurements reported by Hinton et al. (36) differed from measurements for the same rivers in the other compilations. This may be the result of measurements taken at different locations along the same river, or of measurements taken at different times with different flow conditions, some of which may not represent bankfull. Accordingly, where rivers from the Hinton et al. dataset overlapped with others in our broader compilation, only the Hinton et al. data were used for consistency.

The full dataset is provided as an additional supplementary file.

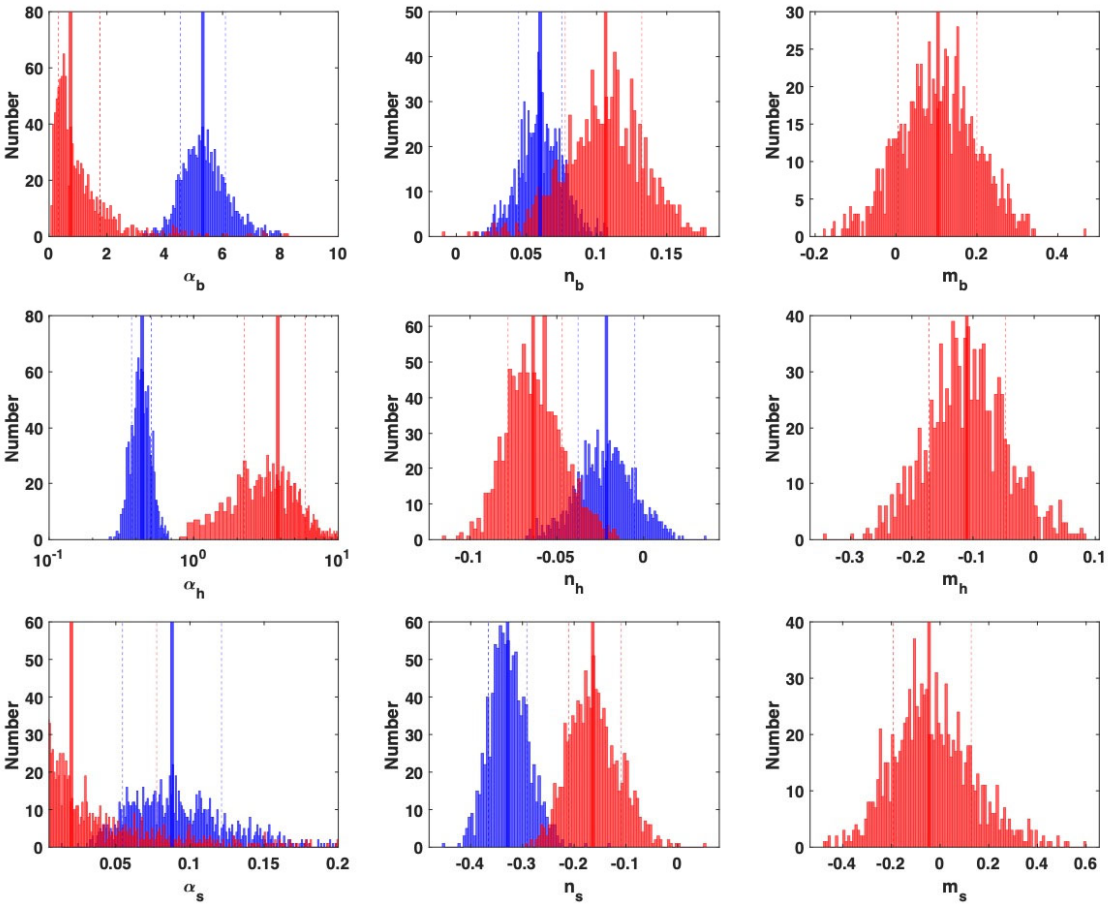

Fig. S1. **Histograms of estimated parameter values in the dimensionless hydraulic geometry relationships for width ($\widetilde{B}$), depth ($\widetilde{H}$) and slope (S) from the Monte Carlo procedure.** Colors are as in Fig. 2 of the main text. Median values are shown by thick vertical lines, and the 16th and 84th percentiles are shown by dashed lines. Bedload-dominated and suspended load-dominated rivers differ significantly from each other for most empirical parameters. All values are reported in Table S2.

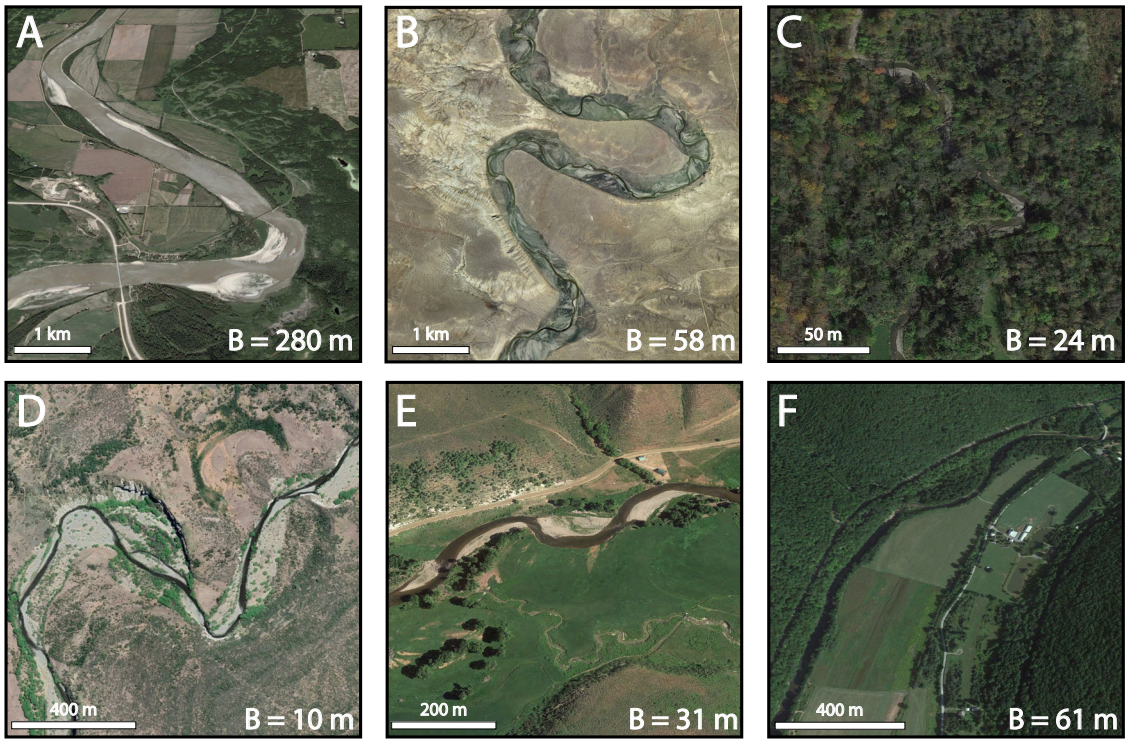

Fig. S2. **Variations in bank material and vegetation among rivers in the terrestrial data compilation.** (A) Smoky River near Watino, Alberta, Canada; (B) Blacks Fork River near Little America, Wyoming, USA; (C) Butternut Creek near Pompey, New York, USA; (D) Cohihues Creek near Esquel, Argentina; (E) Little Snake River near Slater, Colorado, USA; (F) Lycoming Creek near Trout Run, Pennsylvania, USA. All images were acquired from Google Earth.

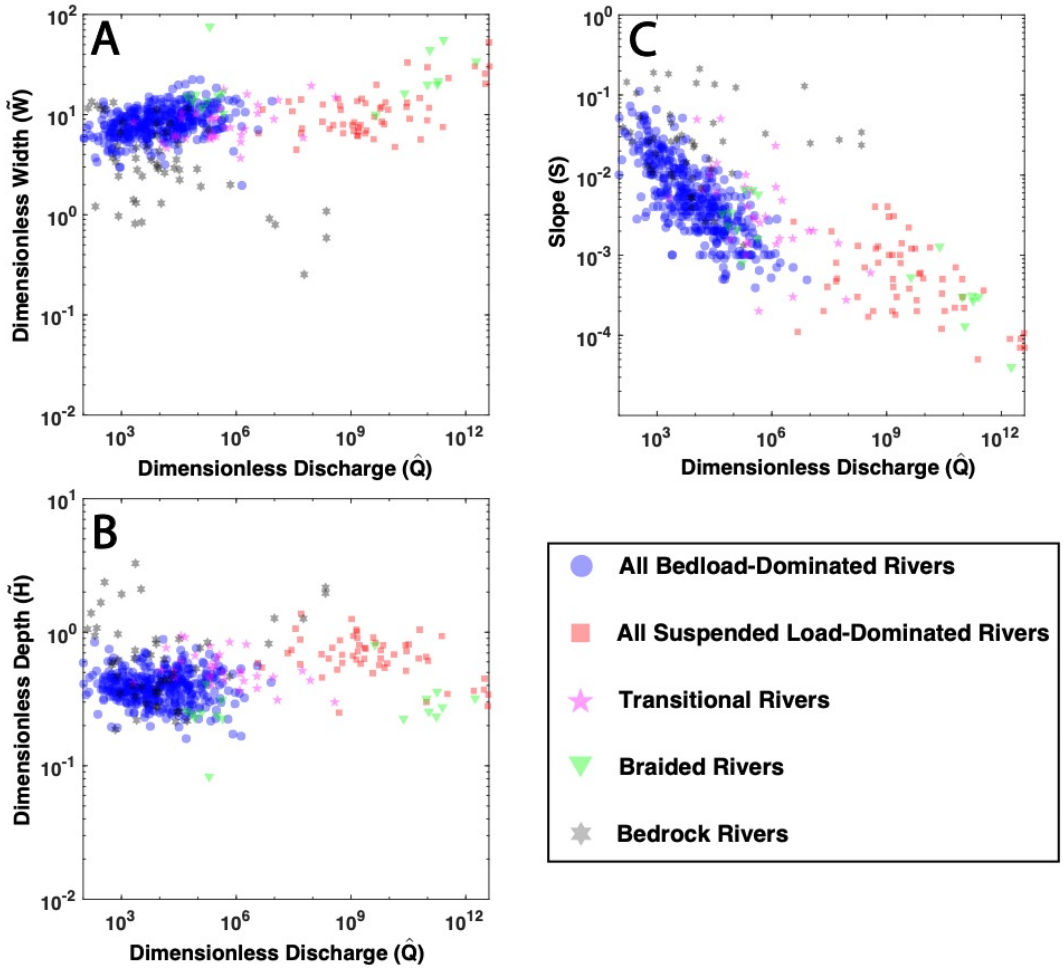

Fig. S3. Dimensionless width ($\tilde{B}$), depth ($\tilde{H}$), and slope (S), as functions of the dimensionless discharge ($\hat{Q}$). This figure is an extension of Fig. 2, with the addition of bedrock rivers, braided rivers, and transitional rivers. Suspended load-dominated and bedload-dominated rivers are not separated according to floodplain characteristics as in Fig. 2, but are instead plotted together for comparison with other river types. Bedrock rivers clearly plot separately from all other river types, indicating different controls on their hydraulic geometry. Braided rivers plot close to bedload-dominated and suspended load-dominated rivers.

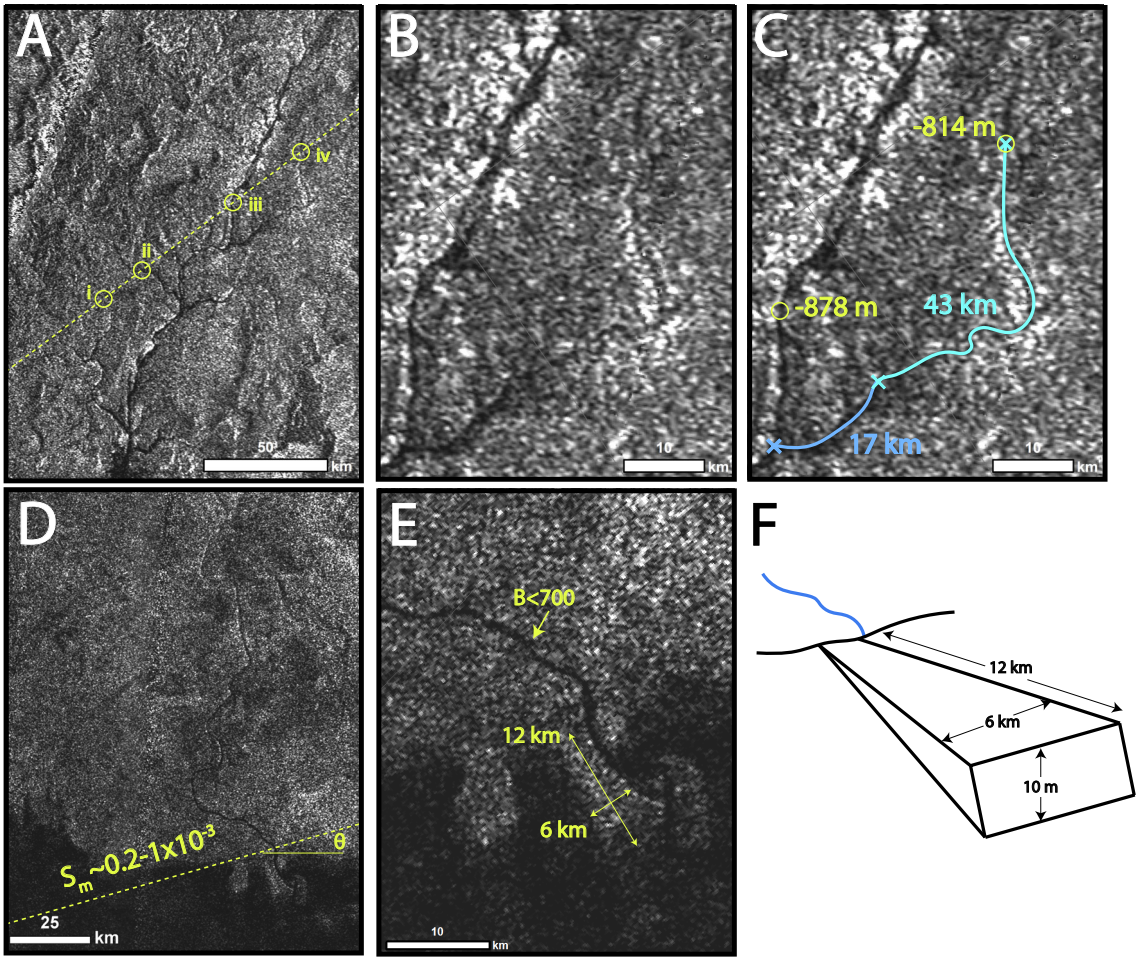

Fig. S4. ***Cassini* SAR images of Vid Flumina and Saraswati Flumen on Titan.** *Cassini* SAR images of Vid Flumina (A) and Saraswati Flumen (D) with the spacecraft ground tracks, where altimetry data (31) were gathered, as yellow dashed lines. At Vid Flumina, the altimeter measured the liquid surface elevations at 4 unique locations (i–iv). (B) Detail of the Vid Flumina tributary of interest. (C) Similar to (B) but with flow path lengths and liquid surface elevations marked as described in Section 2 above. (D) *Cassini* measured the slope of the plain (11) as S_m along a ground track that intersects the shoreline at angle θ. (E) Detail of the delta at the terminus of Saraswati Flumen, with the delta dimensions demarcated. (F) A perspective schematic of how the delta volume was estimated, with horizontal dimensions corresponding to those measured for the sub-aerial portion of the delta lobe in (E).

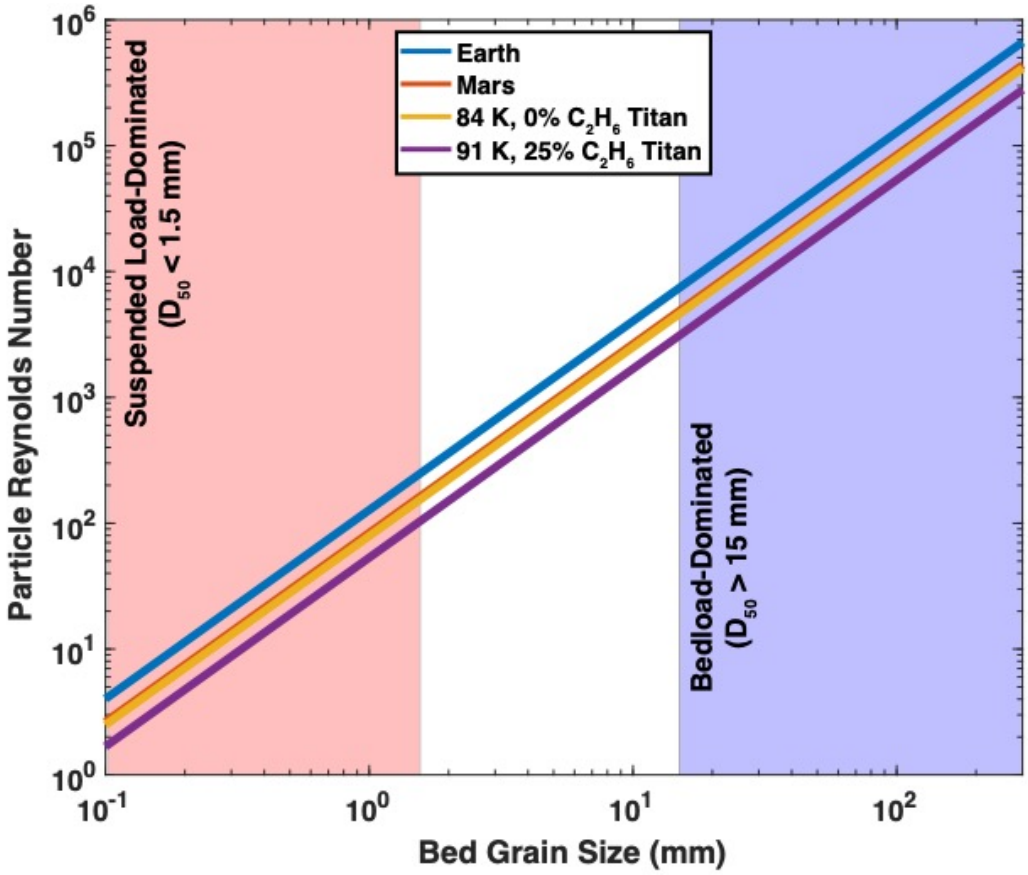

Fig. S5. Particle Reynolds number as a function of grain size on Earth, Mars, and Titan. Fluid and sediment properties are listed in Table S1. For equivalent Re_p, grain size on Titan and Mars is slightly larger than on Earth. The yellow line for colder liquid on Titan partly overlaps the red line for Mars.

Table S1. Physical constants in hydraulic geometry calculations for Earth, Mars, and Titan. Fluid compositions on Titan are a function of the fluid temperature and the ethane mole fraction, reported here as an alkane percentage (from 21). Note that this is not a percentage of the fluid volume, as there are also significant volumes of nitrogen incorporated into the fluid, especially in colder, methane-rich liquids (21).

Physical Parameter	Earth	Mars	Titan [84 K, 0% C_2H_6]	Titan [91 K, 25% C_2H_6]
Sediment Density (ρ_s)	2.65 g/cm^3	2.9 g/cm^3	0.95 g/cm^3	0.95 g/cm^3
Fluid Density (ρ)	1.0 g/cm^3	1.0 g/cm^3	0.67 g/cm^3	0.540 g/cm^3
Fluid Kinematic Viscosity (ν)	0.01 cm^2/s	0.01 cm^2/s	0.003 cm^2/s	0.006 cm^2/s
Gravity (g)	9.81 m/s^2	3.71 m/s^2	1.35 m/s^2	1.35 m/s^2

Table S2. Empirical constants derived from fitting terrestrial alluvial river data. The median of the distribution for each fitted constant from Equation 1, and shown also in Figure 2 and Figure S1, are listed along with the 16th and 84th percentiles.

Empirical Parameter	Bedload-Dominated	Suspended Load-Dominated
α_b	5.2 ± 1.0	$0.70^{+1.1}_{-0.4}$
n_b	0.06 ± 0.02	0.11 ± 0.03
m_b	N/A	0.10 ± 0.09
α_h	0.44 ± 0.06	$3.7^{+2.3}_{-1.6}$
n_h	-0.02 ± 0.02	-0.06 ± 0.02
m_h	N/A	-0.11 ± 0.07
α_s	0.09 ± 0.03	$0.02^{+0.06}_{-0.01}$
n_s	-0.33 ± 0.03	-0.17 ± 0.04
m_s	N/A	-0.05 ± 0.15

Table S3. **Quantities used in hydraulic geometry calculations for Peace Vallis Fan, Gale Crater, Mars.** Values of D_{50}, Q, Q_s, and H were computed as described in the main text. Slopes and widths were measured (35), albeit at different locations on the fan surface. Also shown are the computed runoff rates (M) and active bankfull flow time (t) required to form the deposit, with the latter only considered for the central fan scenario. Drainage area and deposit volume are reported in the main text. All calculations for Peace Vallis Fan only consider that the channels are bedload-dominated, with no washload fraction ($\gamma = 0$). Estimates using the median width are bolded, while ranges for estimates that use the 10th and 90th percentile widths are provided in parentheses.

	Distal fan	Central fan
Slope	$S = 0.003$	$S = 0.01$
Width	$B = 27 \pm 16$ m	
D_{50} (cm)	$\mathbf{4.8}$ $(2.0 - 7.7)$	$\mathbf{26}$ $(11 - 41)$
Q (m^3/s)	$\mathbf{35}$ $(3.7 - 112)$	$\mathbf{60}$ $(6.0 - 190)$
Q_s (m^3/s)	$\mathbf{1.3 \times 10^{-3}}$ $(1.4 \times 10^{-4} - 4 \times 10^{-3})$	$\mathbf{1 \times 10^{-2}}$ $(1 \times 10^{-3} - 0.04)$
H (m)	$\mathbf{1.5}$ $(0.6 - 2.4)$	$\mathbf{1.9}$ $(0.8 - 3.0)$
M (mm/hr)	$\mathbf{0.2}$ $(0.02 - 0.6)$	$\mathbf{0.3}$ $(0.03 - 0.9)$
t (hours)	N/A	$\mathbf{1.5 \times 10^7}$ $(4.6 \times 10^6 - 1.4 \times 10^8)$

Table S4. **Quantities used in hydraulic geometry calculations for the western Jezero delta, Mars.** Values of D_{50}, Q, Q_s, and H were computed as described in the main text. Widths were measured by (38). Slopes for bedload-dominated rivers were measured by (37), who traced stratigraphic boundaries on the delta deposit. For suspended load-dominated scenarios, we only use the lowest slopes from (37), as steeper slopes would be unlikely for such rivers (Materials and Methods). Also shown are the computed runoff rates (M) and active bankfull flow hours (t) required to form the deposit. Drainage area and deposit volume are reported in the main text. Estimates using the median width are bolded, while ranges for estimates that use the 10th and 90th percentile widths are provided in parentheses.

	Bedload-Dominated (low S)	Bedload-Dominated (high S)	Suspended Load-Dominated (low S)
Slope	$S = 0.003$	$S = 0.03$	$S = 0.003$
Width	$B =$ 45 m (19 m and 148 m are the 10th and 90th percentiles)		
D_{50} (cm)	$\mathbf{8}$ $(3.4 - 26)$	$\mathbf{200}$ $(85 - 660)$	N/A
Q (m^3/s)	$\mathbf{125}$ $(15 - 2500)$	$\mathbf{357}$ $(41 - 7000)$	$\mathbf{230}$ $(33 - 3200)$
Q_s (m^3/s)	$\mathbf{4.6 \times 10^{-3}}$ $(5 \times 10^{-4} - 9 \times 10^{-2})$	$\mathbf{2.7 \times 10^{-1}}$ $(3 \times 10^{-2} - 5.4)$	$\mathbf{4 \times 10^{-3}}$ $(5 \times 10^{-4} - 3 \times 10^{-2})$
H (m)	$\mathbf{2.5}$ $(1.1 - 8.3)$	$\mathbf{3.8}$ $(1.6 - 12.6)$	$\mathbf{3.8}$ $(2.0 - 9.1)$
M (mm/hr)	$\mathbf{3.6 \times 10^{-2}}$ $(4 \times 10^{-3} - 7 \times 10^{-1})$	$\mathbf{1.0 \times 10^{-1}}$ $(1 \times 10^{-2} - 2.0)$	$\mathbf{6.6 \times 10^{-2}}$ $(1 \times 10^{-2} - 9 \times 10^{-1})$
t (hours)	$\mathbf{8.8 \times 10^{8}}$ $(5 \times 10^{7} - 8 \times 10^{9})$	$\mathbf{1.5 \times 10^{7}}$ $(8 \times 10^{5} - 1 \times 10^{8})$	$\mathbf{5.1 \times 10^{8}}$ $(5 \times 10^{7} - 3 \times 10^{9})$

Table S5. Quantities used in hydraulic geometry calculations for Saraswati Flumen, Titan. Values of D_{50}, Q, Q_s, and H were computed as described in the main text. Also shown are the computed runoff rates (M) and active bankfull flow time (t) required to form the Ontario Lacus delta. Channel widths and slopes are listed here and in the main text. Calculations were made using fits to both the bedload-dominated rivers (Table S2) and suspended load-dominated rivers (Table S2), and for both a colder, 0% ethane liquid, and a warmer, 25% ethane mole fraction liquid (Table S1).

	Saraswati Flumen [cold, bedload]	Saraswati Flumen [warm, bedload]	Saraswati Flumen [cold, susp. load]	Saraswati Flumen [warm, susp. load]
Slope	$S = 4\times10^{-4}$–0.002			
Width (m)	B = 175 – 700 m			
D_{50} (cm)	$1.6 - 61$	$1.5 - 56$	N/A	N/A
Q (m^3/s)	$35 - 2300$	$100 - 6900$	$680 - 4.5 \times 10^4$	$730 - 4.9 \times 10^4$
Q_s (m^3/s)	$6.5 \times 10^{-4} - 0.36$	$8.9 \times 10^{-4} - 0.49$	$1.2 - 9.4$	$0.43 - 3.3$
H (m)	$1.0 - 5.6$	$1.9 - 10.3$	$6.7 - 26$	$7.2 - 28$
M (mm/hr)	$0.013 - 0.84$	$0.038 - 2.5$	$0.24 - 16$	$0.26 - 18$
t (hours)	$1.8 \times 10^5 - 1.8 \times 10^8$	$1.3 \times 10^5 - 7.3 \times 10^7$	$6.9 \times 10^3 - 5.2 \times 10^4$	$2.0 \times 10^4 - 1.5 \times 10^5$

Table S6. Quantities used in hydraulic geometry calculations for Vid Flumina, Titan. Values of D_{50}, Q, Q_s, and H were computed as described in the main text. Slopes and widths were measured (main text). Also shown are the computed runoff rates (M). Channel widths and slopes are listed here and in the main text. Calculations were made using fits to both the bedload-dominated rivers (Table S2) and suspended load-dominated rivers (Table S2), and for both a colder, 0% ethane liquid, and a warmer, 25% ethane mole fraction liquid (Table S1).

	Vid Flumina [cold, bedload]	Vid Flumina [warm, bedload]	Vid Flumina [cold, susp. load]	Vid Flumina [warm, susp. load]
Slope	0.0011–0.0015			
Width (m)	100 – 175			
D_{50} (cm)	$3.8 - 10$	$3.5 - 9.4$	N/A	N/A
Q (m^3/s)	$14 - 64$	$41 - 190$	$405 - 1700$	$440 - 1900$
Q_s (m^3/s)	$0.96 - 6.7 \times 10^{-3}$	$1.3 - 9.2 \times 10^{-3}$	$0.26 - 0.68$	$0.09 - 0.24$
H (m)	$0.72 - 1.3$	$1.3 - 2.4$	$5.5 - 8.9$	$5.9 - 9.6$
M (mm/hr)	$0.04 - 0.18$	$0.11 - 0.53$	$1.1 - 4.8$	$1.2 - 5.2$

Dataset S1 (separate file). This dataset contains the terrestrial data used in the study, including measurements of channel width, slope, depth, flow discharge and bed grain size for all rivers. Where available, sediment flux measurements and uncertainties are also provided.

References within the Supplementary Information

Numbers below match the main text where overlap exists.

(1) Parker, G., Wilcock, P., Paola, C., and Dietrich, W. (2007). Physical basis for quasi-universal relationships for bankfull hydraulic geometry of single-thread gravel-bed rivers, J. Geophys. Res., 112, F04005.

(2) Wilkerson, G.V., and Parker, G. (2011). Physical basis for quasi-universal relationships for bankfull hydraulic geometry of sand-bed rivers, J. Hydr. Eng., 137, 7.

(3) Parker, G. (2005). Dimensionless Bankfull Hydraulic Relations for Earth and Titan. AGU Fall Meeting.

(4) Hayes, A.G., Lorenz, R.D., and Lunine, J.I. (2018). A post-Cassini view of Titan's methane-based hydrologic cycle. Nature Geoscience, 11, 306-313.

(11) Hayes, A.G., et al. (2011). Transient surface liquid in Titan's polar regions from Cassini. Icarus, 211, 655-671.

(20) Leopold, L.B., and Maddock, T. (1953). The hydraulic geometry of stream channels and some physiographic implications, U.S. Geol. Surv. Prof. Pap., 252, 1-57.

(21) Steckloff, J.K., et al. (2020). Stratification Dynamics of Titan's Lakes via Methane Evaporation. The Planetary Science Journal, 1:26.

(22) Parker, G. (1978a), Self-formed straight rivers with equilibrium banks and mobile bed. Part 1. The sand-silt river, J. Fluid Mech., 89(1), 109–125.

(26) Dunne, K.J., and Jerolmack, D.J. (2020). What sets river width? Science Advances, 6, eabc1505.

(31) Poggiali, V., et al. (2016). Liquid-filled canyons on Titan. Geophys. Res. Lett. 43, 7887–7894.

(35) Palucis, M.C., et al. (2014). The origin and evolution of the Peace Vallis fan system that drains to the Curiosity landing area, Gale Crater, Mars. J. Geophys. Res., 119, 705-728.

(36) Hinton, D., Hotchkiss, R., and Ames, D.P. (2016). Comprehensive and Quality-Controlled Bedload Transport Database. Jour. Hyd. Eng., 143.

(37) Mangold, N., et al. (2021). Perseverance rover reveals an ancient delta-lake system and flood deposits at Jezero crater, Mars. Science, 374, 711-717.

(38) Lapôtre, M.G.A., and Ielpi, A. (2020). The pace of fluvial meanders on Mars and implications for the western delta deposits of Jezero crater. AGU Advances, 1, e2019AV000141.

(59) Wye, L.C. (2011). Radar scattering from Titan and Saturn's icy satellites using the Cassini spacecraft. PhD thesis, Stanford University, Faculty of Engineering.

(66) Dietrich, W.E. (1982). Settling Velocity of Natural Particles. Water Resources Research, 18, 1615-1626.

(74) Pfeiffer, A.M., Finnegan, N.J., and Willenbring, J.K. (2017). Sediment supply controls equilibrium channel geometry in gravel rivers. PNAS, 114, 3346-3351.

(75) Phillips, C.B., and Jerolmack, D.J. (2016). Self-organization of river channels as a critical filter on climate signals. Science, 352, 694-697.

(76) Trampush, S.M., Huzurbazar, S., and McElroy, B. (2014). Empirical assessment of theory for bankfull characteristics of alluvial channels. Water Resources Research, 50, 9211-9220.

(77) Kaless, G., Mao, L. and Lenzi, M.A. (2014). Regime theories in gravel-bed rivers: models, controlling variables, and applications in disturbed Italian rivers. Hydrological Processes, 28, 2348-2360.

(78) Wohl, E., and David, G.C.L. (2008). Consistency of scaling relations among bedrock and alluvial channels. Jour. Geophys. Res., 113, F04013.

(79) Turowski, J.M., Lague, D., and Hovius, N. (2007). Cover effect in bedrock abrasion: A new derivation and its implications for the modeling of bedrock channel morphology. Jour. Geophys. Res. Earth Surface, 112, F4.

(80) Ferrier, K.L., Huppert, K.L., and Perron, J.T. (2013). Climatic control of bedrock river incision. Nature, 496, 206-209.